Acta Mechanica (2003) 0/1083
DOI 10.1007/s00707-003-0064-z

Acta Mechanica
Printed in Austria

A study of size-dependent microindentation

S. H. Chen, C. J. Tao, and **T. C. Wang**, Beijing, China

Received April 28, 2003; revised September 24, 2003
Published online: November 25, 2003

Summary. We recently proposed a strain gradient theory to account for the size dependence of plastic deformation at micron and submicron length scales. The strain gradient theory includes the effects of both rotation gradient and stretch gradient such that the rotation gradient influences the material character through the interaction between the Cauchy stresses and the couple stresses; the stretch gradient measures explicitly enter the constitutive relations through the instantaneous tangent modulus. Indentation tests at scales on the order of one micron have shown that measured hardness increases significantly with decreasing indent size. In the present paper, the strain gradient theory is used to model materials undergoing small-scale indentations. A strong effect of including strain gradients in the constitutive description is found with hardness increasing by a factor of two or more over the relevant range behavior. Comparisons with the experimental data for polycrystalline copper and single crystal copper indeed show an approximately linear dependence of the square of the hardness, H^2, on the inverse of the indentation depth, $1/h$, i.e., $H^2 \propto 1/h$, which provides an important self-consistent check of the strain gradient theory proposed by the authors earlier.

1 Introduction

The indentation hardness of a ductile metal is usually considered to be a measure of its yield stress in compression. According to conventional plasticity theory, in which all material properties are length scale independent, the measured hardness values should be independent of the indentation size. Recently, hardness has been shown to be size-dependent when the width of the impression is below about fifty microns [1]–[4]. The measured hardness may double or even triple as the size of indent decreases from about fifty microns to one micron. In fact, the smaller the scale, the stronger the solid. Similar size effects have been observed for a wide range of plasticity phenomena. For example, thin-wire torsion and micro-thin beam bending have shown that materials display strong size effects when the characteristic length scale is on the order of microns [5], [6]. The strength of particle-reinforced metals increases with decreasing particle diameter at a fixed volume fraction of the particle [7].

The conventional plasticity cannot predict the size dependence. Therefore, new constitutive theories involving a material length are needed in order to characterize and predict such phenomena. Fleck and Hutchinson [8] developed a phenomenological strain gradient theory based on the reduced couple stress theory, and a material length scale was introduced for dimensional grounds. When explaining experimental findings of indentation and fracture, they found it was necessary to introduce two length parameters [9]. One length refers to the rotational gradient as originally proposed in connection with the torsion measurements. The other refers to the stretch gradient, which is needed to rationalize length scale phenomena found in

indentation and fracture. Gao et al. [10] proposed a mechanism-based theory of strain gradient plasticity (MSG).

However, the above strain gradient plasticity theories introduce the higher order stress, which is required for this class of strain gradient theories to satisfy the Clausius-Duhem thermodynamic restrictions on the constitutive model for second deformation gradients [11]. In contrast, no work conjugate of the strain gradient has been defined in the alternative gradient theories [12]–[14]. Retaining the essential structure of conventional plasticity and obeying thermodynamic restrictions, Acharya and Bassani [15] conclude that the only possible formulation is a flow theory with strain gradient effects represented as an internal variable, which acts to increase the current tangent-hardening modulus. In 2000, Chen and Wang [16] established a hardening law based on the incremental version of conventional J_2 deformation theory, which allows the problem of incremental equilibrium equations to be stated without higher-order stress, higher-order strain rate or extra boundary conditions. The new hardening law has been used to investigate microtwisting and microbending experiments. The predictions based on the hardening law agree well with the experimental data. Furthermore Chen and Wang [17] proposed a new rotation gradient theory with independent micro-rotation degrees of freedom, ω_i, which has no relation with the displacement u_i. When the rotation gradient is considered only, the phenomena found in the thin-wire torsion and ultra-thin beam bending tests can be explained successfully. When the fracture and indentation problems are considered, the hardening law proposed in [16] must be used, in which the stretch gradient is introduced. A new kind of strain gradient theory was established [18], which consists of the new rotation gradient theory [17] and the hardening law [16]. The new strain gradient theory [18] was used and successfully explained the cleavage fracture in homogeneous material [19] and bimaterial [20], which was found by Elssener et al. [21]. The size effect in particle-reinforced metal matrix composites [22] is also successfully investigated by the new strain gradient theory [18].

The indentation problem has been investigated with several strain gradient theories. Shu and Fleck [23] failed to explain the indentation behavior using the strain gradient theory proposed by Fleck et al. [8] to analyze the indentation test, because only the rotation gradient is considered. Begley and Hutchinson [24] used the theory proposed by Fleck and Hutchinson [9] to determine the effect of the material length scale on the predicted hardness for small indents. Huang et al. [25] used the MSG theory to analyze this kind of problem, a linear dependence of the square of the hardness, H^2, on the inverse of the indentation depth, $1/h$, i.e., $H^2 \propto 1/h$ is obtained.

In the present paper, the recently proposed strain gradient theory [18], [19] will be used to investigate the microindentation hardness tests. This study will serve as an important consistency check of the present theory. The strain gradient theory [18], [19] is summarized in Sect. 2. In Sect. 3, the indentation problem is investigated for the new strain gradient theory by means of the finite element method. Finite element formulas are given and the method of dealing with the contact problem will be shown in this section. The indentation model and comparisons of the numerical results and the experimental data are presented in Sect. 4.

2 Summary of strain gradient theory

The strain gradient theory proposed by Chen and Wang [18], [19] is briefly reviewed here. In a Cartesian reference frame x_i, the strain tensor ε_{ij} and the stretch gradient tensor η_{ijk} [26] are related to the displacement u_i by

$$\varepsilon_{ij} = \frac{1}{2}(u_{i,j} + u_{j,i}), \quad \eta_{ijk} = u_{k,ij}. \tag{1}$$

The rotation gradient is related to the independent micro-rotation vectors ω_i,

$$\chi_{ij} = \omega_{i,j}. \tag{2}$$

The effective strain, effective rotation gradient and effective stretch gradient are defined as

$$\varepsilon_e = \sqrt{\frac{2}{3}\varepsilon'_{ij}\varepsilon'_{ij}}, \quad \chi_e = \sqrt{\frac{2}{3}\chi'_{ij}\chi'_{ij}}, \quad \eta_1 = \sqrt{\eta^{(1)}_{ijk}\eta^{(1)}_{ijk}}, \tag{3}$$

where ε'_{ij}, χ'_{ij} are the deviatoric parts of the counterparts, and the definition of $\eta^{(1)}_{ijk}$ can be found in [26].

The constitutive relations are as follows:

$$\sigma_{ij} = \frac{2\Sigma_e}{3E_e}\varepsilon'_{ij} + K\varepsilon_m\delta_{ij}, \quad m_{ij} = \frac{2\Sigma_e}{3E_e}l_{cs}^2\chi'_{ij} + K_1 l_{cs}^2\chi_m\delta_{ij}, \tag{4}$$

$$\begin{cases} E_e^2 = \varepsilon_e^2 + l_{cs}^2\chi_e^2 & \Sigma_e = (\sigma_e^2 + l_{cs}^{-2}m_e^2)^{1/2}, \\ \sigma_e^2 = \frac{3}{2}s_{ij}s_{ij} & m_e^2 = \frac{3}{2}m'_{ij}m'_{ij}. \end{cases} \tag{5}$$

E_e is called the effective generalized strain and Σ_e is the work conjugate of E_e; l_{cs} is an intrinsic material length, which reflects the effects of the rotation gradient on the material behaviors; K is the volumetric modulus and K_1 is the bend-torsion volumetric modulus.

In order to consider the influence of the stretch gradient, the new hardening law [16] is introduced,

$$\begin{cases} \dot{\Sigma}_e = A'(E_e)\left(1 + \frac{l_1\eta_1}{E_e}\right)^{\frac{1}{2}}\dot{E}_e = B(E_e, l_1\eta_1)\dot{E}_e & \Sigma_e \geq \sigma_Y, \\ \dot{\Sigma}_e = 3\mu\dot{E}_e & \Sigma_e < \sigma_Y, \end{cases} \tag{6}$$

where $B(E_e, l_1\eta_1)$ is the hardening function; l_1 is the second intrinsic material length associated with the stretch gradient, σ_Y is the yield stress and μ the shear modulus.
The equilibrium relations in V are

$$\sigma_{ij,j} = 0, \quad m_{ij,j} = 0. \tag{7}$$

The traction boundary conditions for force and moment are

$$\sigma_{ij}n_j = T_i^0 \quad \text{on } S_T, \quad m_{ij}n_j = q_i^0 \quad \text{on } S_q. \tag{8}$$

The additional boundary conditions are

$$u_i = u_i^0 \quad \text{on } S_u, \quad \omega_i = \omega_i^0 \quad \text{on } S_\omega. \tag{9}$$

It is an assumption that the term $\left(1 + \frac{\rho_G}{\rho_s}\right)^{1/2}$ in Chen and Wang's theory is characterized by $\left(1 + \frac{l_1\eta_1}{E_e}\right)^{1/2}$. According to MSG theory, it should be $\left[1 + \frac{l_1\eta_1}{f^2(E_e)}\right]^{1/2}$, we tried to use this formula to investigate the thin-wire torsion and thin beam bending in Chen and Wang's strain gradient theory. Unfortunately, the theoretical results were not consistent with experimental results. While we use the term $\left(1 + \frac{l_1\eta_1}{E_e}\right)^{1/2}$ in our theory, the results were good.

One should note that at each incremental step both the effective strain ε_e and the effective stretch gradient η_1 could be obtained from the updated displacement fields u_i; the effective rotation gradient χ_e can be obtained from the updated rotation fields ω_i. Hence, η_1 is an internal parameter in Eq. (6), and it doesn't invoke higher-order stress or higher-order strain rates.

When the stretch gradient is introduced, Eq. (6) is in the incremental form in order to ensure that there is no higher-order stress associate with the stretch gradient. The constitutive relations are written in the incremental form:

$$\begin{cases} \dot{\sigma}_{ij} = 2\mu\dot{\varepsilon}'_{ij} + K\dot{\varepsilon}_m\delta_{ij} \\ \dot{m}_{ij} = 2\mu l_{cs}^2\dot{\chi}'_{ij} + K_1 l_{cs}^2\dot{\chi}_m\delta_{ij} \end{cases}, \qquad \Sigma_e < \sigma_Y \tag{10}$$

$$\begin{cases} \dot{\sigma}_{ij} = \dfrac{2\Sigma_e}{3E_e}\dot{\varepsilon}'_{ij} + \dfrac{2\dot{\Sigma}_e}{3E_e}\varepsilon'_{ij} - \dfrac{2\Sigma_e}{3E_e^2}\varepsilon'_{ij}\dot{E}_e + K\dot{\varepsilon}_m\delta_{ij} \\ \dot{m}_{ij} = \dfrac{2\Sigma_e}{3E_e}l_{cs}^2\dot{\chi}'_{ij} + \dfrac{2\dot{\Sigma}_e}{3E_e}l_{cs}^2\chi'_{ij} - \dfrac{2\Sigma_e}{3E_e^2}l_{cs}^2\chi'_{ij}\dot{E}_e + K_1 l_{cs}^2\dot{\chi}'_{ij}\delta_{ij} \end{cases}, \quad \Sigma_e \geq \sigma_Y \tag{11}$$

where Σ_e is the integration of $\dot{\Sigma}_e$ and $\dot{\Sigma}_e$ is expressed by Eq. (6).

3 Finite element formulation

In this section, the finite element formulas are presented for the new strain gradient theory. The principle of virtual work requires

$$\int_V (\sigma_{ij}\delta\varepsilon_{ij} + m_{ij}\delta\chi_{ij})dV = \int_S (t_k\delta u_k + q_k\delta\omega_k)dS, \tag{12}$$

where V and S are the volume and surface of the material, respectively. The virtual strains $\delta\varepsilon_{ij}$ are related to the virtual displacements δu_k via Eq. (1) and $\delta\chi_{ij}$ are related to the virtual rotation vector $\delta\omega_k$. t_k is surface stress traction and q_k is the surface torque traction.

The displacement field can be interpolated by the element shape functions N_i and the nodal displacements. Similarly, the micro-rotation field can be obtained through interpolating the element shape functions N_i and the nodal rotation vectors. The strains and strain gradients can be obtained from the kinematic relations (1)–(3). The stresses are then obtained via the constitutive relations of Eq. (4). The nodal displacements and rotation vectors have to be solved incrementally due to the new incremental hardening law, i.e. Eq. (6). Therefore, the nodal displacements and the rotation vectors are solved for each loading step by rewriting the principle of virtual work Eq. (12) about the current solution as

$$\begin{aligned} &\int_V (\Delta s_{ij}\delta\varepsilon'_{ij} + \Delta\sigma_m\delta\varepsilon_{kk} + \Delta m'_{ij}\delta\chi'_{ij} + \Delta m_m\delta\chi_{kk})dV - \int_S (\Delta t_k\delta u_k + \Delta q_k\delta\omega_k)dS \\ &\quad = -\int_V (s_{ij}\delta\varepsilon'_{ij} + \sigma_m\delta\varepsilon_{kk} + m'_{ij}\delta\chi'_{ij} + \Delta m_m\delta\chi_{kk})dV + \int_S (t_k\delta u_k + q_k\delta\omega_k)dS, \end{aligned} \tag{13}$$

where the superscript prime denotes the deviatoric quantities, Δ on the left-hand side stands for increments, whereas the right-hand side involves the current quantities.

3.1 The nodal degrees of freedom

It is convenient to express the field quantities in terms of the circular cylindrical coordinate system (r, θ, z) as shown in Fig. 1. Both the geometry and loading are axis-symmetric, and without loss of generality we consider the section $\theta = 0$. The indented solid is subjected to the displacement field

$$u_r = u_r(r,z), \quad u_\theta = 0, \quad u_z = u_z(r,z) \tag{14}$$

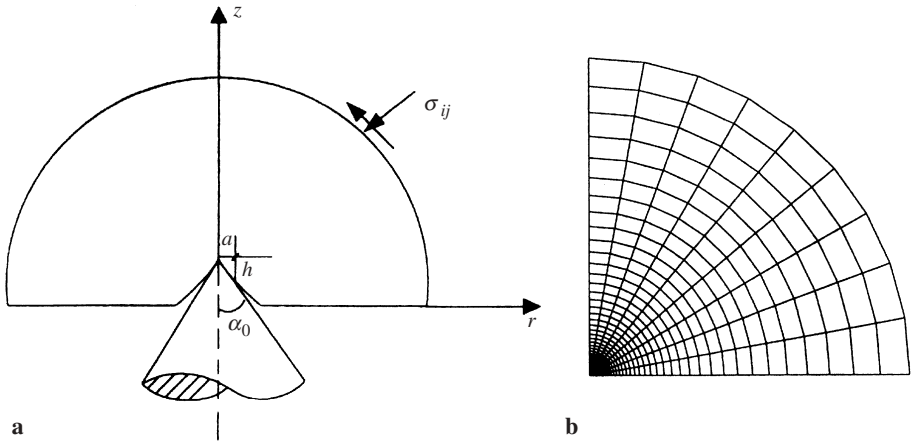

Fig. 1a. Geometry of the axis-symmetric indentation model and boundary conditions; **b** Finite element calculation model

and the micro-rotation field

$$\omega_\theta = \omega_\theta(r,z) \quad \omega_r = \omega_z = 0. \tag{15}$$

Due to the independent parameter ω_i is introduced in addition to the displacement u_i in the present strain gradient theory, which is different from the theory proposed by Fleck and Hutchinson [8], one node has three degrees of freedom, i.e., u_{ir}, u_{iz} and $\omega_{i\theta}$ for the axis-symmetric indentation case. The displacement field and the rotation vector field can be obtained through the shape function and the nodal displacement and nodal rotation vectors, i.e.,

$$u_r = \sum_{i=1}^{n} N_i u_{ir}, \tag{16}$$

$$u_z = \sum_{i=1}^{n} N_i u_{iz}, \tag{17}$$

$$\omega_\theta = \sum_{i=1}^{n} N_i \omega_{i\theta}. \tag{18}$$

3.2 The components of strain gradient

The components of stretch strain gradient terms can be obtained from the current nodal displacements through the shape functions. For the axis-symmetric case they can be written as

$$\begin{cases} \eta_{rrr} = \sum\limits_{i=1}^{m} \frac{\partial^2 N_i}{\partial r^2} u_{ri} & \eta_{rrz} = \sum\limits_{i=1}^{m} \frac{\partial^2 N_i}{\partial r^2} u_{zi}, \\ \eta_{r\theta\theta} = \eta_{\theta r\theta} = \eta_{\theta\theta r} = \frac{1}{r}\sum\limits_{i=1}^{m} \frac{\partial N_i}{\partial r} u_{ri} - \frac{\sum\limits_{i=1}^{m} N_i u_{ri}}{r^2} & \\ \eta_{rzr} = \eta_{zrr} = \sum\limits_{i=1}^{m} \frac{\partial^2 N_i}{\partial r \partial z} u_{ri} & \eta_{zzz} = \sum\limits_{i=1}^{m} \frac{\partial^2 N_i}{\partial z^2} u_{zi}, \\ \eta_{rzz} = \eta_{zrz} = \sum\limits_{i=1}^{m} \frac{\partial^2 N_i}{\partial r \partial z} u_{zi} & \eta_{\theta\theta z} = \frac{1}{r}\sum\limits_{i=1}^{m} \frac{\partial N_i}{\partial r} u_{zi}, \\ \eta_{\theta z\theta} = \eta_{z\theta\theta} = \frac{1}{r}\sum\limits_{i=1}^{m} \frac{\partial N_i}{\partial z} u_{ri} & \eta_{zzr} = \sum\limits_{i=1}^{m} \frac{\partial^2 N_i}{\partial z^2} u_{ri}, \end{cases} \tag{19}$$

where N_i is the shape function and m is the node number of the element; u_{ri} and u_{zi} are the i-th nodal displacements in the directions of the x-axis and z-axis, respectively.

3.3 Choice of element

Many researchers [22], [23], [27], [28] have found that the choice of the element for gradient plasticity is complicated and in particular quite sensitive to details of the constitutive relation. Xia and Hutchinson [27] have discussed some choices of finite elements for strain gradient plasticity with the emphasis on plane strain cracks. Several elements have been developed for the phenomenological theory of strain gradient plasticity to investigate the crack tip field, microindentation experiments and stress concentrations around a hole.

In order to consider the strain gradient, the constant strain element is excluded since there is no strain gradient in this kind of element. For the two-dimensional case, such as the problem of plane strain and the axis-symmetry, a second-order element can be used, such as the eight-node and nine-node elements. In the present paper, a nine-node element has been used to analyze the indentation problem. The displacement and rotation vectors in the element are interpolated through the shape function, whereas the strain and the rotation gradient tensors in the element are then obtained via Eq. (1) and Eq. (2). This element is only suitable for solids with vanishing higher-order stress traction on the surface. For example, the element has worked very well in the fracture analysis of strain gradient plasticity [28], where the higher-order stress tractions vanish on the crack face and on the remote boundary. This element also works well in the study of microindentation experiments [25] because the higher-order stress tractions are zero on the indented surface. Since the new strain gradient theory does not include higher-order stress and higher-order stress tractions, these kinds of elements will work well in the present study of axis-symmetric indentation as discussed in the next section.

3.4 Assumptions in the numerical simulation

The assumptions made in the present calculation are: (i) The indenter is assumed to be axis-symmetric, which greatly simplifies the finite element analysis. This assumption has been adopted by previous strain gradient plasticity analyses of micro-indentation experiments. Furthermore, we simulate a conical indenter shown in Fig. 1. The half-angle of the indenter is taken to be $\alpha_0 = 72^\circ$, corresponding to a Vickers indenter. The displacement at the tip of indentation is δ, whereas the contact radius of the indentation is a. (ii) We assume that the indenter is frictionless such that there is no sticking between the indenter and the substrate.

3.5 Calculation model

In this section, the indentation calculation model is not the same as those in all other references. The elastic stress field corresponding to the indentation of classical elastic theory is loaded on the outer boundary as shown in Fig. 1, and the tip of the indenter is assumed to be static. (r, θ, z) is the cylindrical coordinate and (R, θ, φ) is the spherical coordinate for the cross section as shown in Fig. 1. The materials are compressed to slide up and down the face of the indenter by the outer stress field loaded on the external boundary of the materials. In Fig. 1, there are the following relations:

$$R^2 = r^2 + z^2, \quad r = R\sin\varphi, \quad z = R\cos\varphi, \tag{20}$$

$$\begin{cases} \sigma_r = \dfrac{P}{2\pi R^2}\left[\dfrac{1-2v}{1+\cos\varphi} - 3\sin^2\varphi\cos\varphi\right] \\ \sigma_z = \dfrac{-3P}{2\pi R^2}\cos^3\varphi \\ \sigma_{rz} = \dfrac{-3P}{2\pi R^2}\sin\varphi\cos^2\varphi \\ \sigma_\theta = \dfrac{(1-2v)P}{2\pi R^2}\left[\cos\varphi - \dfrac{1}{1+\cos\varphi}\right]. \end{cases} \tag{21}$$

The outer elastic field σ_{ij} loaded on the outer boundary in Fig. 1 denotes the stress components σ_{RR} and $\sigma_{\varphi R}$, which can be obtained from Eq. (21). The couple stresses loading on the outer boundary are

$$m_{RR} = 0, \quad m_{\varphi R} = 0, \quad m_{\theta R} = 0. \tag{22}$$

Due to the vanishing couple stress on the outer boundary, the independent rotation vectors in this problem vanish, from where one can see that the rotation gradient has no effect on the indentation problem and the results will only be influenced by the stretch gradient. The value of the length scale l_{cs} will not be considered. Only the length scale related to the stretch gradient, l_1, will be taken as a parameter.

3.6 Boundary condition

Since the calculation model in the present paper is different from other existing models, the boundary conditions are different from them, too. The displacement u_r is zero along the axis of symmetry, where (r,z) are cylindrical coordinates. The displacement u_z at the point of the indenter tip is also zero. The elastic stress field is loaded on the external boundary and the couple stress field vanishes on the outer boundary. The contact boundary conditions are added to simulate the real indent process as follows.

The contact between the indenter and indented material is simulated by assuming a contact radius a of indentation, and iterating to find the proper outer elastic stress field in order to satisfy the normal stress traction t_n at the periphery of contact vanishing as shown in Fig. 2,

$$t_n|_{r<a} < 0, \quad t_n|_{r\geq a} = 0, \tag{23}$$

where the subscript n denotes the normal of the contact face.

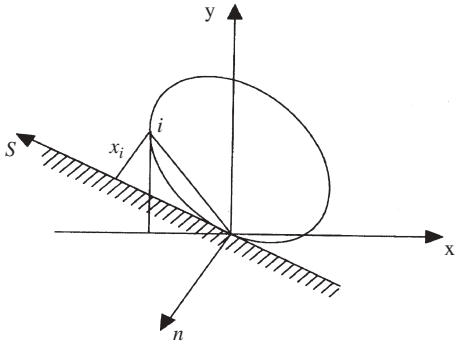

Fig. 2. Contact model for the calculation in the present paper

The contact boundary is assumed to be frictionless, i.e.,

$$t_s = 0, \tag{24}$$

where the subscript S denotes the tangent of the contact face.

On the contact boundary, the face torque vanishes, too. The displacement u_r of the points on the contact boundary is not constrained a priori, which is different from all other existing calculation models, i.e. u_r of the contact points is the natural calculated outcome for the present model. The points on the contact boundary must be ensured to stay on the contact face, i.e.,

$$u_z = -(r + u_r)\mathrm{ctg}\,\alpha_0 = -r^*\mathrm{ctg}\,\alpha_0, \tag{25}$$

where $r^* = r + u_r$, r is the coordinate of each node on the contact boundary before deformation, and r^* is the corresponding coordinate after deformation.

If one point goes beyond the contact face, it must be drawn back to the contact face as shown in Fig. 2, i.e., $x_i < 0$, the point must be drawn back and render $x_i \geq 0$.

It should be pointed out also that for both pile-up and sink-in, the periphery of the contact between the indenter and the indented material is governed by Eq. (25) and Eq. (23). Therefore, pile-up or sink-in is not imposed a priori, but a natural outcome of the indentation analysis.

The relation between the contact radius a and the plastic depth of indentation h is given by

$$h = \frac{a}{\tan\alpha_0}, \tag{26}$$

where $\alpha_0 = 72^\circ$ is a half angle of the indenter as shown in Fig. 1.

The total force, P, exerted on the indenter is the sum of nodal forces in the z direction for those nodes in contact with the indenter (i.e., $r \leq a$). The indentation hardness H is defined as

$$H = \frac{P}{\pi a^2}. \tag{27}$$

4 Numerical results for indentation

4.1 Deformation characteristics

In this section, the numerical results are shown in the following. First, the classical plasticity theory, i.e., the intrinsic length scales $l_1 = l_{cs} = 0$, is used to calculate the indentation, and the indented material is perfectly elastic-plastic material, we find that the hardness is almost 3 times the yield stress, which proves that the finite element program is correct.

For power-law hardening materials, the deformed surface under the indenter is shown in Fig. 3 for different contact radius. In this figure, the radius and vertical locations have been normalized by the material length scale l_1, which is assumed to be a material property. It must be noted that in Fig. 3 the radius r^* for each point is the original coordinate r plus the displacement u_r of this point, and in the following figures r^* has the same meaning. From Fig. 3, we find that for the same hardening exponent, the larger the contact radius, the larger the external loading but the smaller the hardness.

In Fig. 4, the normalized vertical displacements near the contact face are shown with the same contact radius and different hardening exponent n. From Fig. 4, we could find that while the indented material tends to be an elastic one, pile-up will transfer to be sink-in, which denotes that hard material tends to sink-in and soft material tends to pile up. It is consistent with all experimental observations.

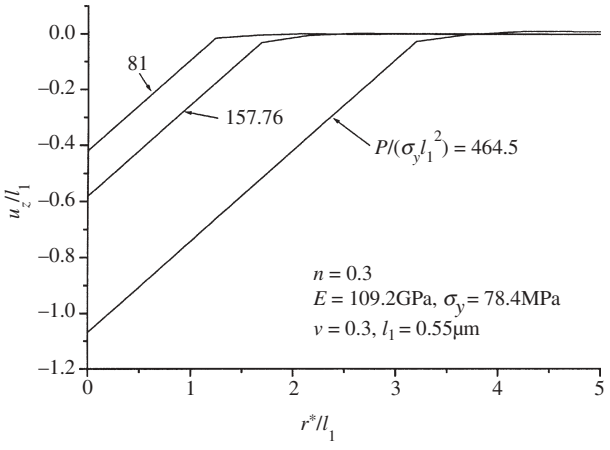

Fig. 3. Deformed surface profiles for several indenter sizes and contact material length scales. Given in the figure are normalized values of the indent load

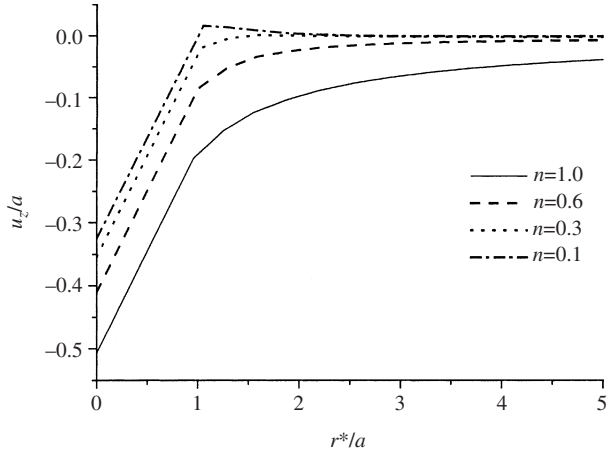

Fig. 4. The normalized surface displacements due to indentation by a frictionless conical indenter for different hardening exponents

The normalized vertical displacements near the contact face for the same indented material but two kinds of theories, i.e., the classical plasticity theory and the strain gradient theory, are shown in Fig. 5. From Fig. 5, we find that for the same contact radius the hardness with strain gradient is larger than that without strain gradient and pile-up transfers to be sink-in while the effect of strain gradient is considered, which means that the strain gradient considered will render the material stiffer. It is consistent well with the results in [24].

4.2 Comparison with experiment

In this section, the exponential hardening law is used for the polycrystalline copper and single-crystal copper when no strain gradient effects are considered. The conventional hardening law is as follows:

$$\sigma_e = E\varepsilon_e, \quad \varepsilon_e < \varepsilon_0, \tag{28}$$

$$\sigma_e = \sigma_0 \varepsilon_e^n, \quad \varepsilon_e \geq \varepsilon_0. \tag{29}$$

From the above equations, we can obtain the yield stress σ_y,

$$\sigma_y = \left(\frac{\sigma_0}{E^n}\right)^{\frac{1}{1-n}}. \tag{30}$$

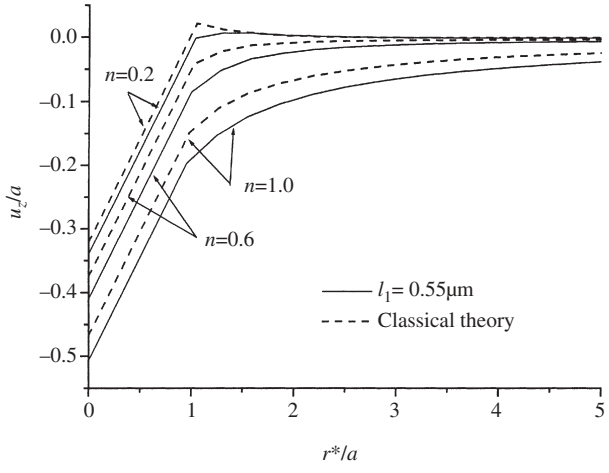

Fig. 5. The normalized surface displacements for both the strain gradient theory proposed by Chen and Wang [18], [19] and the classical theory

The indentation hardness calculated by the finite element method for the strain gradient theory and indentation model in the previous sections are presented as following. In particular, we focus on the comparisons between the experimentally measured microindentation hardness data for polycrystalline copper and single crystal copper given by McElhaney et al. [2] and the numerical calculation hardness data obtained in this paper.

From the experimental data given in [2], we know that the plastic work-hardening exponent for polycrystalline copper is $n = 0.3$. Other material parameters are Young's modulus $E = 109.2$ GPa, the shear modulus $\mu = 42$ GPa, Poisson ratio $v = 0.3$. While the indent depth is very large, i.e., the influence of the strain gradient becomes very small, the hardness of the polycrystalline copper is $H_0 = 834$ MPa. Combining the experimental data given in [2] and the hardness, we obtain the reference stress $\sigma_0 = 688$ MPa, and the yield stress is $\sigma_Y = 78.4$ MPa.

Figure 6a presents the microindentation hardness predicted by the present strain gradient theory, $(H/H_0)^2$, versus the inverse of the indentation depth, $1/h$, for polycrystalline copper, where H is the microindentation hardness, $H_0 = 834$ MPa is the indentation hardness without the strain gradient effect and h is the depth of indentation. Figure 6b shows the relation between the normalized indentation hardness, H/H_0, versus the inverse of the square root of the indentation depth, $1/h^{1/2}$. The experimental data given by McElhaney et al. [2] are also presented in Fig. 6a and b for comparison. It is clearly observed that the predicted hardness based on the present strain gradient theory agrees very well with the experimentally measured microindentation hardness data over a wide range of indentation depth, from $0.1\,\mu$m to several microns when $l_1 = 0.55\,\mu$m. Furthermore, the numerical results based on the present strain gradient theory do give an approximate straight line in Fig. 6a, which is consistent with the estimate by Nix and Gao [29]. While in Fig. 6b, instead of linearity, a relatively complex function, approximately a parabolic relation, exists between H/H_0 and $1/h^{1/2}$, due to which simple linear relation between $(H/H_0)^2$ and $1/h$ is used commonly for describing the size effects in microindentation.

We also analyze the single-crystal copper. The reference stress is $\sigma_0 = 436$ MPa and the work hardening exponent $n = 0.3$, Poisson's ratio $v = 0.3$. Young's modulus is $E = 109.2$MPa. The yield stress is $\sigma_y = 41$ MPa. The hardness in a large-scale test is $H_0 = 581$ MPa, i.e., the hardness without strain gradient effects.

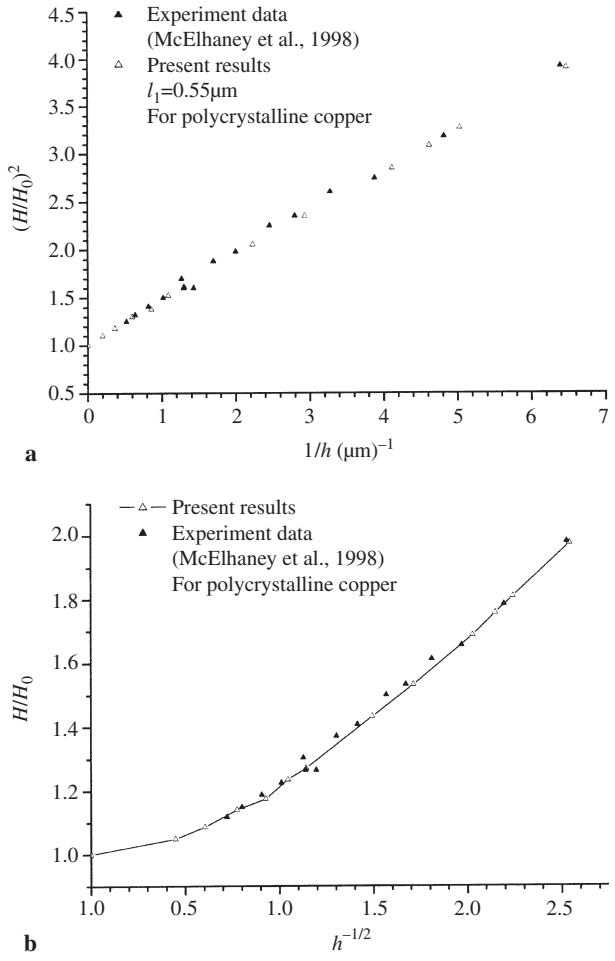

Fig. 6. Dependence of the normalized hardness on the indentation contact depth for polycrystalline copper and comparisons of the numerical results with the experimental results; **a** Relation between $(H/H_0)^2$ and $1/h$; **b** Relation between H/H_0 and $1/h^{1/2}$

Figure 7a shows the normalized numerical calculation hardness data predicted by the present strain gradient theory, $(H/H_0)^2$, versus the inverse of the indentation depth, $1/h$, for single-crystal copper. The relation between the normalized indentation hardness, H/H_0, versus the inverse of the square root of the indentation depth, $1/h^{1/2}$, is shown in Fig. 7b. The experimentally measured hardness data are also shown in Fig. 7a and b in order to compare with the numerical results. From Fig. 7, one can see that the predicted hardness based on the present strain gradient theory agrees very well with the experimentally measured microindentation hardness data over a wide range of the indentation depth, from $0.1\,\mu$m to several microns when $l_1 = 2.1\,\mu$m. The relation between $(H/H_0)^2$ and $1/h$ is almost linear, which is also consistent well with the estimate by Nix and Gao [29]. Also, an approximately parabolic relation exists between H/H_0 and $1/h^{1/2}$ in Fig. 7b.

Figure 8a shows the relation between the square of the normalized indentation hardness, $(H/H_0)^2$, and the inverse of the square root of the contact area, $1/\sqrt{A}$, for polycrystalline copper. The relation between the normalized indentation hardness, H/H_0, and $A^{-1/4}$, is shown in Fig. 8b. Experimental results with the corresponding relations for polycrystalline copper are also shown both in Fig. 8a and b for comparison. From the two figures, one can see that a

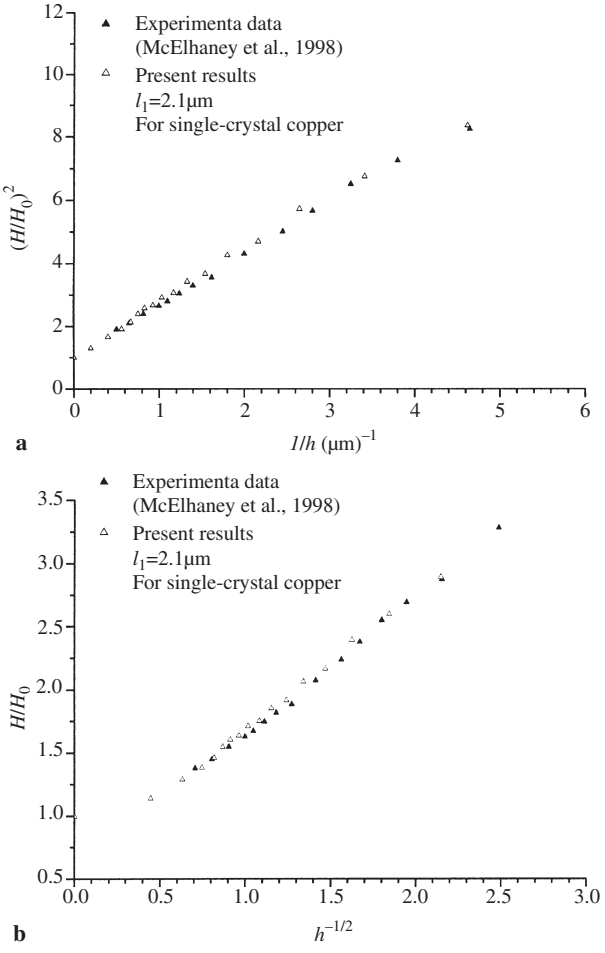

Fig. 7. Dependence of the normalized hardness on the indentation contact depth for single-crystal copper and comparisons of the numerical results with the experiment results; **a** Relation between $(H/H_0)^2$ and $1/h$; **b** Relation H/H_0 and $1/h^{1/2}$

linear function describes the relation between $(H/H_0)^2$ and $1/\sqrt{A}$ and a nonlinear relation exists between H/H_0 and $A^{-1/4}$, which can be proved from the relations between $(H/H_0)^2$ and $1/h$ since $\sqrt{A}$ has the same dimension as h. The relations for single crystal copper between $(H/H_0)^2$ and $1/\sqrt{A}$ and that between H/H_0 and $A^{-1/4}$ are shown in Fig. 9a and b, respectively. The corresponding relations existing between these two groups of variables are the same as those in Fig. 8a and b.

The agreements between the predicted hardness based on the present strain gradient theory and the experimentally measured microindentation hardness in Figs. 6–9 provide a validation of the present theory. Both the numerical analysis and the microindentation experiments show approximately linear dependences of the square of the indentation hardness on the inverse of the indentation depth, which is an important result obtained also by [29]. However, nonlinear relations exist between H/H_0 and $1/h^{1/2}$ or between H/H_0 and $A^{-1/4}$. The agreements between the numerically predicted results and the experimental results serve as a self-consistent check of the present strain gradient theory.

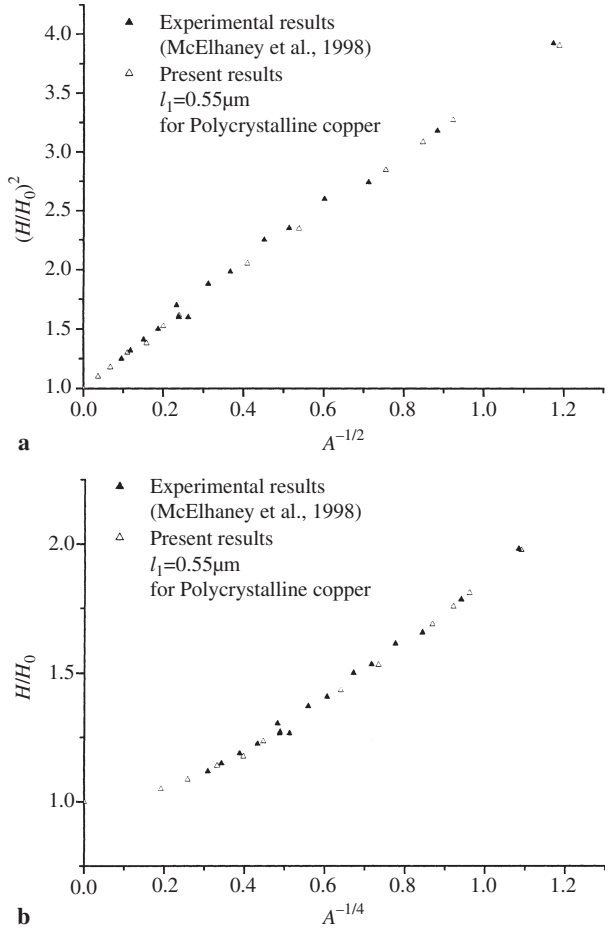

Fig. 8. Dependence of the normalized hardness on the contact area for polycrystalline copper and comparisons of the numerical results with the experimental results; **a** Relation between $(H/H_0)^2$ and $1/\sqrt{A}$; **b** Relation between H/H_0 and $A^{-1/4}$

5 Concluding remarks

We have shown that the recently proposed strain gradient theory by Chen and Wang reproduced the linear dependence of the square of indentation hardness on the inverse of the indentation depth observed in microindentation experiments. A rigorous finite-element analysis of microindentation experiments is performed, and the results show a good agreement with the indentation hardness data. The length scale related to the stretch gradient is predicted. This study validates the strain gradient theory proposed by Chen and Wang as a new theory of Mechanics, which can easily analyze engineering problems for advanced microscale materials technology.

Acknowledgements

This work is supported by the National Science Foundation of China (Nos. 10202023 and 10272103) and Excellent Post-doctoral Research-Starting Fund of CAS.

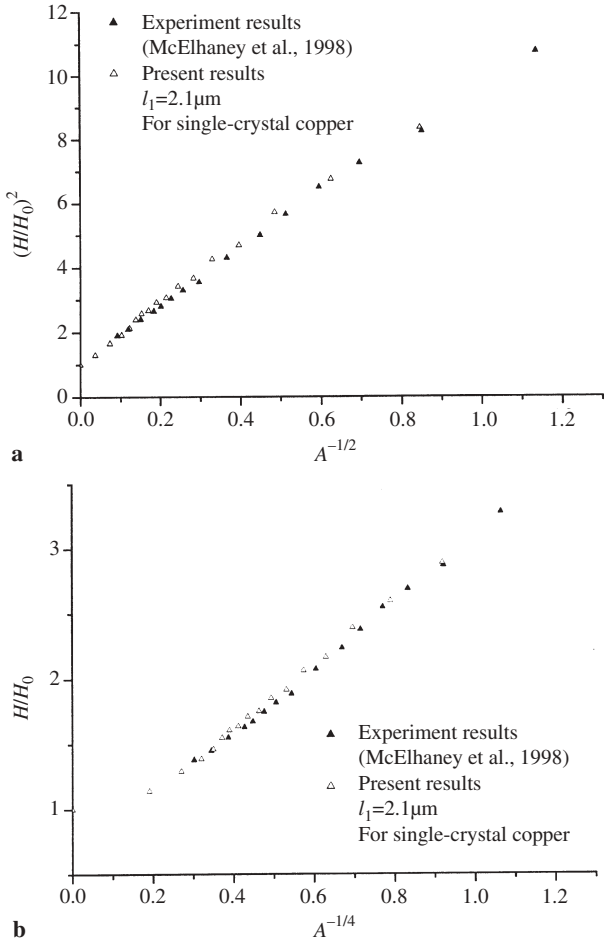

Fig. 9. Dependence of the normalized hardness on the contact area for single-crystal copper and comparisons of the numerical results with the experimental results; **a** Relation between $(H/H_0)^2$ and $1/\sqrt{A}$; **b** Relation between H/H_0 and $A^{-1/4}$

References

[1] Ma, Q., Clarke, D. R.: Size dependent hardness in silver single crystals. J. Mater. Res. **10,** 853–863 (1995).

[2] McElhaney, K. W., Vlassak, J. J., Nix, W. D.: Determination of indenter tip geometry and indentation contact area for depth-sensing indentation experiments. J. Mater. Res. **13,** 1300–1306 (1998).

[3] Nix, W. D.: Mechanical properties of thin films. Metall. Trans. **20A,** 2217–2245 (1989).

[4] Poole, W. J., Ashby, M. F., Fleck, N. A.: The role of strain gradients in grain size effect for polycrystals. J. Mech. Phys. Solids **44,** 465–495 (1996).

[5] Fleck, N. A., Muller, G. M., Ashby, M. F., Hutchinson, J. W.: Strain gradient plasticity: theory and experiment. Acta Metal. Mater. **42,** 475–487 (1994).

[6] Stolken, J. S., Evans, A. G.: A microbend test method for measuring the plasticity length scale. Acta Mater. **46,** 5109–5115 (1998).

[7] Lloyd, D. J.: Particle-reinforced aluminum and magnesium matrix composite. Int. Mater. Rev. **39,** 1–23 (1994).

[8] Fleck, N. A., Hutchinson, J. W.: A phenomenological theory for strain gradient effects in plasticity. J. Mech. Phys. Solids **41,** 1825–1857 (1993).

[9] Fleck, N. A., Hutchinson, J. W.: Strain Gradient Plasticity. Adv. Appl. Mech. **33** (Hutchinson, J. W., Wu, T. Y., eds.), pp. 295–361. New York: Academic Press 1997.

[10] Gao, H., Huang, Y., Nix, W. D., Hutchinson, J. W.: Mechanism-based strain gradient plasticity-I. Theory. J. Mech. Phys. Solids **47,** 1239–1263 (1999).

[11] Acharya, A., Shawki, T. G.: Thermodynamic restrictions on constitutive equations for second-deformation-gradient inelastic behavior. J. Mech. Phys. Solids **43,** 1751–1772 (1995).
[12] Aifantis, E. C.: On the microstructural origin of certain inelastic models. Trans. ASME J. Eng. Mater. Technol. **106,** 326–330 (1984).
[13] Muhlhaus, H. B., Aifantis, E. C.: The influence of microstructure-induced gradients on the localization of deformation in viscoplastic materials. Acta Mech. **89,** 217–231 (1991).
[14] Zbib, H., Aifantis, E. C.: On the gradient-dependent theory of plasticity and shear banding. Acta Mech. **92,** 209–225 (1992).
[15] Acharya, A., Bassani, J. L.: On non-local flow theories that preserve the classical structure of incremental boundary value problems. In: Micromechanics of plasticity and damage of multiphase materials. IUTAM Symposium, Paris, August 29–September 1, 1995.
[16] Chen, S. H., Wang, T. C.: A new hardening law for strain gradient plasticity. Acta Mater. **48,** 3997–4005 (2000).
[17] Chen, S. H., Wang, T. C.: A new deformation theory for strain gradient effects. Int. J. Plast. **18,** 971–995 (2002).
[18] Chen, S. H., Wang, T. C.: Strain gradient theory with couple stress for crystalline solids. European J. Mech. A/Solids **20,** 739–756 (2001).
[19] Chen, S. H., Wang, T. C.: Finite element solutions for plane strain mode I crack with strain gradient effects. Int. J. Solids Struct. **39,** 1241–1257 (2002).
[20] Chen, S. H., Wang, T. C.: Interface crack problem with strain gradient effects. Int. J. Fract **117,** 25–37 (2002).
[21] Elssener, G., Korn, D., Ruehle, M.: The influence of interface impurities on fracture energy of UHV diffusion bonded metal-ceramic bicrystals. Scripta Metall. Mater. **31,** 1037–1042 (1994).
[22] Chen, S. H., Wang, T. C.: Size effects in the particle-reinforced metal-matrix composites. Acta Mech. **157,** 113–127 (2002).
[23] Shu, J. Y., Fleck, N. A.: The prediction of a size effect in microindentation. Int. J. Solids Struct. **35,** 1363–1383 (1998).
[24] Begley, M. R., Hutchinson, J. W.: The mechanics of size-dependent indentation. J. Mech. Phys. Solids **46,** 2049–2068 (1998).
[25] Huang, Y., Xue, Z., Gao, H., Nix, W. D., Xia, Z. C.: A study of micro-indentation hardness tests by mechanism-based strain gradient plasticity. J. Mater. Res. **15,** 1786–1796 (2000).
[26] Smyshlyaev, V. P., Fleck, N. A.: The role of strain gradients in the grain size effect for polycrystals. J. Mech. Phys. Solids **44,** 465–495 (1996).
[27] Xia, Z. C., Hutchinson, J. W.: Crack tip fields in strain gradient plasticity. J. Mech. Phys. Solids **44,** 1621–1648 (1996).
[28] Wei, Y., Hutchinson, J. W.: Steady-state crack growth and work of fracture for solids characterized by strain gradient plasticity. J. Mech. Phys. Solids **45,** 1253–1273 (1997).
[29] Nix, W. D., Gao, H.: Indentation size effects in crystalline materials: a law for strain gradient plasticity. J. Mech. Phys. Solids **46,** 411–425 (1998).

Authors' address: S. H. Chen, C. J. Tao, and T. C. Wang, LNM, Institute of Mechanics, Chinese Academy of Sciences, Beijing 100080, China (E-mail: chenshaohua72@hotmail.com)